Supporting Information

Kim et al. 10.1073/pnas.1323632111

SI Materials and Methods

Bacterial Strains and Growth Conditions. *Pseudomonas fluorescens* Pf0-1 is a soil isolate (1), the WT parent strain of all mucoid variants isolated and described in this study (Table S1). One of the mucoid variants was randomly chosen as the prototype and designated as MV. All routine cloning was done in *Escherichia coli* 10B (Invitrogen), and *E. coli* S17.1λ*pir* (2) was used as the donor strain in conjugations. *P. fluorescens* strains were routinely grown in *Pseudomonas* minimal medium (PMM) (3) at 30 °C and *E. coli* strains in Luria Broth (LB) at 37 °C, or as stated otherwise. Liquid cultures were shaken in test tubes at 250 rpm. The evolution of mucoid variants is observed in minimal and complex media supplemented with glycerol or glucose as carbon source. King's Medium B (KMB) (4) or *Pseudomonas* agar F (PAF, a commercial formulation of KMB) was used as the base for detailed evolution and competition analyses. When necessary, a given medium was solidified with agar [1.5% (wt/vol)] and supplemented with the following antibiotics: ampicillin (100 μg/mL), kanamycin (50 μg/mL), streptomycin (50 μg/mL), or gentamicin (30 μg/mL). Complex media components were Difco-branded and obtained from BD and all other chemicals were obtained from Sigma.

Measurement of Growth. For measurement of growth on agar, 20-μL overnight cultures were spotted and absorbed onto the surface of PAF medium (25 mL per plate), which was left to dry for 1 d at room temperature before inoculation. Plates were incubated at room temperature and colonies were harvested over time into test tubes containing 5 mL PBS using bent-glass Pasteur pipettes. Cell suspensions were vortexed until clumps were no longer visible and then serially diluted (10-fold) in fresh PMM and enumerated on PMM-agar. For measurement of growth in liquid, overnight cultures were diluted into KMB and optical density at 600 nm was measured over 24–48 h (30 °C, constant shaking) in the Bioscreen C MBR (Oy Growth Curves Ab) or the Infinite M200 PRO (Tecan).

Competition Experiments. Overnight cultures (1.5 mL) were washed in fresh PMM and resuspended in 1.0 mL PMM. Suspensions were serially diluted accordingly in PMM and mixed with equal volumes of the competing strain suspension. Each mixture was serially diluted and plated out on antibiotic plates to estimate the initial population size of the competing strains. For competition experiments on agar, colonies were spotted using 20 μL of the mixture on PAF plates, incubated, and harvested as described above. Resulting cell suspensions were serially diluted in PMM and enumerated on PMM-agar plates supplemented with streptomycin or kanamycin. For competition experiments in liquid, 20 μL of the mixture was inoculated into test tubes containing 2 mL of KMB or PAF with the agar subtracted. The tubes were either left standing undisturbed in tube racks or shaken at 250 rpm. The liquid cultures were enumerated over time by serially diluting 50-μL samples and plating on PMM-agar plates containing streptomycin or kanamycin. Competition experiments were also set up using fluorescently tagged strains and visualized over time by various imaging procedures described below. The outcome of each competition was analyzed by comparing both the raw CFU data and calculating the relative fitness (W) (5), or as noted otherwise.

Spatial Disruption Experiments. Competition experiments were set up on PAF plates as described above, but the colonies were disrupted by mixing or padding. For the mixing experiment, the colonies were either left alone or disturbed daily: either using a pipette tip (repeated horizontal and vertical motions) or a sterile plastic loop (repeated orbital motion) to physically mix the colony. For the padding experiment, the colonies were either left alone or covered by a thin layer of agarose [3% (wt/vol), prepared between two layers of sterile plastic under pressure]. Fluorescently tagged strains were used in both mixing and padding experiments and each colony was visualized under a fluorescent microscope after 4 d of incubation. Strains tagged with antibiotic resistance were also used in mixing experiments, and the colonies were enumerated on PMM-agar plates supplemented with kanamycin or streptomycin, as described above.

Genome Sequencing and Identification and Confirmation of the Causal Mutation. Genomic DNA from one variant was sequenced to identify the causal mutation that leads to the MV phenotype. Genomic DNA was isolated and purified using the Genomic-tip 100/G, Genomic DNA Buffer Set, lysozyme, proteinase K, and RNase A, as instructed by the manufacturer in the Genomic DNA Handbook (Qiagen). Genomic DNA samples were submitted to the Washington University Genome Sequencing Center (St. Louis, MO) for 454 FLX random fragment library construction and sequencing. Greater than 87 Mbp of sequence data were retrieved with an average read length of 224 bp, representing ~14× genome coverage. Contigs were aligned against the published *P. fluorescens* Pf0-1 genome sequence (6) using the EagleView software (7) and sequences compared using BLAST (8). More than 50 individual cases of sequence mismatches were observed in the dataset; however, the majority were associated with homopolymeric sequences and were thus filtered out, leaving five candidates. A single nucleotide (A) deletion at the 126th position of the coding DNA sequence of the *rsmE* gene was chosen as the primary candidate because its homologs had already been implicated in modulating social behavior in bacteria (9). To confirm the presence of the deletion mutation, *rsmE* and its flanking regions in both the WT and MV were PCR-amplified using primers csrA1 (5′-TTGCGCATCCACACTCTTGC) and csrA2 (5′-GGTGGGGGAATGGCAATACG), and both strands sequenced using internal primers csrA1B (5′-TTCGCCACATCCTGCCAATG) and csrA2B (5′-TCATTGGCGCGCAGGCAAAC). The single-nucleotide deletion was confirmed to be present in the MV but not in WT. The Phusion High-Fidelity DNA Polymerase (Finnzymes) was used in all PCR reactions described in this study unless stated otherwise.

Mutant Construction and Tagging. The gene splicing by overlap extension (SOE) method (10) was used as previously outlined (11) to create mutations in *rsmE* by homologous recombination. The 126th nucleotide (A) of the *rsmE* gene was deleted in the WT by introducing the appropriate mutation in the SOE primers: rsmEpm5f (5′-CAGCAGGCGCCGTTACTACC) and rsmEpm5r (5′-GCTGGTAGATCTCTTCCCGGTGACTGCAACGTTCTTCGGAGC) for the 5′ fragment and rsmEpm3f (5′-GCTCCGAAGAACGTTGCAGTCACCGGGAAGAGATCTACCAGC) and rsmEpm3r (5′-GAAGATGGCGTTGTTCGTGC) for the 3′ fragment. The entire *rsmE* gene was deleted in WT using primers rsmEd5f (5′-ACAAAGCCGTGCTCGATCAG) and rsmEd5r (5′-GGCTACTGACTGCGATAGGGCGGTCTTCTCCTTGATTGCTTTGTAGG) for the 5′ fragment and rsmEd3f (5′-CCTACAAAGCAATCAAGGAGAAGACCGCCCTATCGCAGTCAGTAGCC) and rsmEd3r (5′-GGTGTTGCTCATCACTGGCG)

for the 3′ fragment. Platinum Taq DNA Polymerase High Fidelity (Invitrogen) was used in the PCR reactions to facilitate the downstream T-A cloning process. The two fragments in each set were joined and cloned into the pGEM-T Easy vector system (Promega) then subcloned into the EcoRI site of the suicide plasmid pMQ30 (12). Primers rsmE1 (5′-CGCTGGCATCCTTGATGACG) and rsmE2 (5′-TCTGGATCCGGTGAGGTCGC) were used to monitor the replacement of the WT *rsmE* gene with the mutant constructs by PCR and subsequently confirmed by sequencing both strands as described above. The single-nucleotide deletion strain was named *rsmE*pm and the complete deletion strain was named Δ*rsmE*. The entire *fliC* gene was deleted in MV in the same manner as above using primers fliCd5f (5′-GCTGCAAGGCTGGATAGACG) and fliCd5r (5′-CGCCAAAACTCATTCCGAAACCATGACGAATTCCTCGTTGG) for the 5′ fragment and fliCd3f (5′-CCAACGAGGAATTCGTCATGGTTTCGGAATGAGTTTTGGCG) and fliCd3r (5′-ACTTGCCATGTGCATCTCCC) for the 3′ fragment. Primers fliC1 (5′-ACCCATGCCGGCTGGAGTGATG) and fliC2 (5′-TTGCACCGATGTCCAGGCCG) were used to confirm the deletion of the *fliC* gene. The mini*Tn*7 system was used to tag the chromosomes of the strains used in this study using established procedures. Strains used in competition experiments were tagged with neutral kanamycin or streptomycin resistance cassettes (13). These specific markers allow the identification of the different genotypes of *P. fluorescens* Pf0-1 within mixed populations while not affecting the relative fitness of cells (14). Strains used in microscopy were tagged with GFP, YFP, or DsRed-Express proteins (15). All primers used in this study were obtained from Integrated DNA Technologies and Sanger-based sequencing was carried out by GENEWIZ or Source BioScience. DNA fragments were purified using the QIAquick Kit (Qiagen) and plasmids were extracted using the QIAprep Kit (Qiagen). All enzymes were purchased from New England Biolabs.

Colony and Biosurfactant Spreading Assay on Polycarbonate Membranes. Nuclepore polycarbonate membrane (90- to 142-mm diameter, 0.4-μm pore size; Whatman) was laid on top of PAF plates using sterile forceps, and overnight cultures (2 μL for the mutant library from the parallel evolution experiments, or 20 μL for individual analyses) were spotted on top of the membrane. One side of the membrane appears smooth and shiny whereas the other side appears matted and dull. According to Whatman, the apparent differences stem from the manufacturing process where the duller side faces the open air and the shinier side makes constant contact against the preparatory surface. These physical properties persist across the scale of both phase-contrast and atomic force microscopy, where the surface of the dull side is significantly less uniform to that of the shiny side. Plates were inverted after the spots had been adsorbed and incubated at room temperature.

Measurement of Colony Density. The height (Z) of fluorescently tagged colonies was measured across the diameter (X) in reference to the agar surface by confocal microscopy. The Z dimension was calibrated to one edge of the colony (i.e., single layer of cells) and measurements were made in 0.5-mm increments of X across the center of the colony to the other edge. Given that there were small differences in Z between the two edges, the slope of the base was calculated and each measured Z value across the colony was normalized accordingly. This generated a cross-sectional map across the center of the colony (i.e., Z dimension for the y axis and X dimension for the x axis), which was relatively symmetric. The cross-section was sliced into individual trapezoids (triangles for the two edges) for each X increment from the edges to the center. Each slice was converted into rectangles by keeping the X constant, and cylindrical volume was calculated as a function of the radius (X). Final volume was calculated by averaging the measurements obtained from each half of the cross-section. Following the confocal analysis, each colony was harvested and the population size estimated by serial dilutions and plating as described above. The mean density from three independent colonies was calculated as CFU/mm^3 for each day.

Individual-Based Simulations. An individual-based simulation framework was used that captures bacterial growth and the concentration gradients of oxygen originating from diffusion and bacterial consumption. The parameters used in the simulations are summarized in Table S3. Fifty hours of growth was simulated for a cross-section of a bacterial colony initially seeded with 413 WT and 22 MV cells (i.e., initial relative frequency of MV is 0.05). As observed in our experiments, both cell types were assumed to grow equally fast. We extended an established framework that had been developed and tested over the last 15 y to understand and predict the behavior of bacterial communities. Recently, such simulations have been applied to understand the evolution and ecology of microbial groups (16–20), which have subsequently been validated experimentally (21, 22). The model assumptions, justifications, and implementation are extensively discussed elsewhere (23–26). Briefly, bacterial cells are modeled as growing and dividing spheres that metabolize oxygen in a continuous concentration field that is updated for each iteration by solving the 2D reaction-diffusion equations to steady state using a multigrid solver. Cell growth is calculated by solving the Monod equation based on the local oxygen concentration. We have focused on oxygen as the only nutrient for cells because both in simulations with explicit calculation of glycerol diffusion from the agar and consumption in the colony, as well as in empirical studies (27, 28), oxygen has been found to be the key limiting factor for growth in a colony. In the simulation, oxygen originates from the air above the colony and the agar below and diffuses through a thin diffusion layer (10 μm) above the colony and the agar (simulated thickness is 250 μm, and a constant boundary condition with fixed, low oxygen concentration further below) (Table S3). Cells grow, divide and, in case of MV cells, secrete polymers modeled as inactive spheres. Growth, division and polymer secretion leads to pushing away neighboring cells and expansion of the colony. We considered two patterns of cell division. The first was to assume that cells that divide produce new cells in a random direction. However, observations of the colonies revealed frequent vertical alignment of rod-shaped *P. fluorescens* cells at the interface between the genotypes (Fig. S2*A*). Therefore, we also tested the effects of simulated vertical cell division by enforcing a rule that newborn cells are placed either below or above the mother cell. This assumption of cell division direction does not affect conclusions as both reveal conditions where secretor cells have an evolutionary advantage over nonsecretor cells (Fig. 3 and Fig. S3). However, stochastic loss of genotypes was more likely in the random model, which did not reflect our observations that rare lineages often persist in the colonies. We, therefore, focused on the vertical alignment model (Fig. 3), which also better reflects the microscopy.

Parallel Evolution Experiments. Overnight WT cultures (20 μL) were spotted on PAF plates and incubated for 4 d at room temperature until mucoid variants became clearly visible. A single variant was randomly isolated from each single WT colony, with one exception being that three spatially separated patches of variants were isolated from a common WT colony. Each variant was purified and phenotype confirmed on fresh PAF plates. The *rsmE* locus and its flanking regions were sequenced in each variant by using primers csrA1/2 and csrA1B/2B, as described above.

Statistical Analyses. Given that the sample sizes were too small ($n = 3$) for the Mann–Whitney test, a two-tailed t test was used to compare the relative fitness differences between any two given strains. A Kruskal–Wallis test was applied to compare the relative fitness of the constructed *rsmE* mutants to MV. A Kruskal–Wallis test, corrected for multiple comparisons (Tukey's honestly significant difference criterion), was used to compare CFU ratios of different mucoid variants to the WT. A two-tailed Mann–Whitney test was applied to compare the emergence ratios of different mucoid variants. The Wilcoxon signed-rank test was applied to compare relative fitness in the simulations. Bonferoni correction was applied when making multiple pairwise comparisons, and the relevant values for the n and α parameters are indicated for each test where appropriate. All statistical tests were conducted using Matlab.

Imaging. Still pictures of colonies were generated using the CanoScanLiDE 200 flatbed scanner (Canon) or the EOS 30D DSLR camera (Canon), and images were scaled to calibrated dimensions using the ImageJ software (29). Fluorescently tagged strains were imaged using the Typhoon 9400 scanner (GE Healthcare) and the associated ImageQuant TL software as described elsewhere (30), the SteREO Lumar.V12 microscope (Zeiss) under the NeoLumar S 0.8× objective lens and the associated AxioVision software, or the Axio Zoom.V16 microscope (Zeiss) under the PlanApo Z 0.5× objective lens and the associated Zen software. Confocal imaging was carried out on the LSM 700 laser scanning microscope (Zeiss) using the 20× and 50× objectives and the associated Zen software. A square piece of agar containing the entire colony was cut out and placed on slides without a coverslip for confocal imaging. For all other imaging procedures, entire plates were imaged without disturbing the agar surface.

SI Text

Estimation of the Timeline *of rsmE* Mutations. To estimate the timeline of mutations in *rsmE*, we compared the onset of MV emergence in pure WT colonies (i.e., natural) relative to colonies spiked with a small number of GFP-tagged MV (MVG) cells. Competition experiments were set up on PAF plates between WT and MVG using mixtures set at the following ratios (WT:MVG): $1{:}1 \times 10^{-6}$, $1{:}2 \times 10^{-6}$, and $1{:}3 \times 10^{-6}$. The control group consisted of an equal volume of dH_2O rather than the MVG suspension in the mixtures. The GFP-tagging procedure used in this study renders MVG resistant to gentamicin (15), so the population size of WT and MVG in each inoculate was estimated by serially diluting and plating out the mixture on PMM-agar plates with or without gentamicin supplementation.

Colonies were monitored daily under the fluorescent microscope over a period of 6 d and the results are summarized in Fig. S1*H*. As expected, all mucoid patches that emerged from the initially pure WT populations were nonfluorescent. The spiked fluorescent mucoid cells (i.e., MVG) emerge as visible patches after 2 d, reach their peak on the third day, and plateau thereafter. In contrast, very few nonfluorescent mucoid patches are visible after 3 d in both pure and spiked WT populations, and these then continue to increase in frequency gradually throughout the duration of the experiment. This finding implies that new MV cells emerge from WT in the MV-WT competitions and likely reduce the fitness differences measured at later time points (Fig. 1).

Spiking in a known number of fluorescent mucoid cells also allows us to estimate the probability that a particular mucoid variant cell will successfully form a patch and emerge from the surface of the colony. Specifically, we can compare the relative proportions of the introduced MVG cells that emerge from the WT population as discrete mucoid patches. Measurements made at three different initial frequencies revealed that ~50% of introduced MVG consistently emerge as independent patches (Fig. S1*I*). These data will include some cases where a single mucoid patch emerges from a mixture of multiple MVG cells that happened to start near one another. However, this effect does not seem to be important because we observe strikingly similar proportions of emergence across competitions commenced at different relative frequencies. A cell that harbors the causal mutations thus appears to have a very good chance of emerging as an independent mucoid patch. Collectively, these results suggest that the causal mutations most likely occur de novo in each experiment after the WT populations are seeded on the plates, and are subsequently selected for independently.

Individual-Based Simulation of WT-MV Competitions. Previous theory on the use of polymers in competition for the growing edge was based on liquid submerged biofilms rather than colonies. We therefore modified our individual-based simulation system to capture the competition of a mucoid strain, which makes a bulky secretion that spaces out cells, versus a nonproducer in a colony setting. Parameters for the simulation came from measured values in our experiment and the literature (Table S3). Consistent with studies that measure oxygen levels and growth patterns within colonies (27, 28, 31–33), the key limiting nutrient in the model was found to be oxygen rather than the carbon source, so we focused our analysis on access to oxygen.

The simulation shows that, as for submerged biofilms, secreting strains can have a competitive advantage (Fig. 3 and Fig. S3). However, we found that lateral expansion is more important in colonies relative to upwards expansion, which is the dominant benefit in submerged biofilms. This lateral expansion allows a strain to conquer the region near the surface of the colony where there is best access to oxygen diffusing from above. The strength of this evolutionary advantage was not as great as that seen in the experiments, so we may not capture all of the processes at play. Nevertheless, the simulation demonstrates that our model for secretion-driven expansion can indeed provide an evolutionary advantage in colonies.

Comparison of Rates Between the Emergence of Mucoid Variants and Mutations in *rsmE*. The data presented in Fig. S1*H* was further probed to assess whether the rate of emergence was in accordance with the predicted mutation rates. Mucoid colonies emerging from WT control populations were cumulatively scored over the duration of the experiments and the mean estimates gathered from three independent experiments were used in the calculations. We observed 37 mucoid colonies emerging from each of the WT populations following 6 d of incubation. Experiments that seeded a known number of GFP-labeled *rsmE* mutant cells into colonies indicate that approximately half emerge from the surface in any experiment (Fig. S1*I*). Therefore, the number of loss-of-function *rsmE* mutants arising in the average experiment is ~80.

The size of the initial WT population was 3.05×10^6 CFU, which expanded to 1.89×10^{10} CFU after 6 d, representing $\sim 1.89 \times 10^{10}$ individual replication events. The genome size of the WT strain *P. fluorescens* Pf0-1 is 6.43×10^6 bp (6), so the effective genome size is 1.28×10^7 bp because both strands are copied during each replication event. The mutation rate during a genome replication event (5.40×10^{-10} mutations per base pair per generation) is widely perceived to be similar among bacteria (34). Incorporating this as a proxy for the mutation rate in our experimental system, we estimate the total number of mutations accumulated over the duration to be: $(1.89 \times 10^{10}) \times (1.28 \times 10^7) \times (5.40 \times 10^{-10}) = 1.31 \times 10^8$. The fact that this number is larger than the size of the genome generates an expectation that every nucleotide in the genome will be mutated in at least one cell during the course of the experiment. Although this is only a crude estimate, it gives an idea of the extreme levels

of genetic variability present in the colony. For *rsmE* specifically, given its size of 195 bp (a 3.02×10^{-5} proportion of the genome) the expected number of mutations in *rsmE* based upon the genome average mutation rate is ~4,000 per experiment. Comparison of this expectation with the observation of around 80 *rsmE* mutants per experiments would suggest that mutation rate at *rsmE* is if anything below the genome average. However, this comparison rests upon the incorrect assumption that every mutation in *rsmE* leads to a loss of function. Thus, it is necessary to correct the genome-based estimate of *rsmE* mutation rate for the proportion of mutations that will cause a loss of function.

The goal then is to determine the effective target size for *rsmE*, which can be estimated by multiplying the size of the gene by the probability that any given mutation will result in the mucoid phenotype. Our estimations are based on the methods described by Lang and Murray (35) using the collection of mutations identified in this study (Table S1). The collection comprises 212 insertions and deletions (collectively referred to as "indels") and 322 base pair substitutions (BPS). The 31 mutations (7 indel and 24 BPS) identified solely in the 5′ untranslated region are excluded from calculations because it is not possible to meaningfully predict the probability of loss of function mutations outside the coding sequence.

We have identified 11 unique (40 in total) nonsense substitutions, which represent 79% of the 14 possible nonsense substitutions in *rsmE*. There are 26 unique substitutions within the collection of 282 missense mutations. Under the assumption that the same proportion of missense substitutions was isolated as in the nonsense collection, we predict that $14/11 \times 26 = 33$ possible missense mutations will result in loss of function. This result gives a total of $14 + 33 = 47$ BPS mutations that will lead to loss of function. In comparing these mutations with all possible BPS in *rsmE*, we must also consider the fact that each base can mutate to three different base pairs so each specific mutation event is only one of three options for its particular position. Therefore, we divide the number of nonsense and missense substitutions by three to generate an effective number of base pairs that will result in a loss of function; this leads to an estimate of 16 base pairs (τ_{BPS}), which is the *rsmE*-specific target size for all BPS. Moving to indels, under the assumption that any insertion or deletion is deleterious to RsmE and thus produces the mucoid phenotype, the *rsmE*-specific target size for indels is 195 base pairs (τ_{indels}).

To combine τ_{BPS} and τ_{indels} into a single effective target size, we must next estimate the relative probability that a mutation results in a BPS versus an indel. We can do this using the distribution of BPS (322 of 534 = 60%) and indels (212 of 534 = 40%) in our mutant collection. Notably, the overrepresentation of BPS relative to indels is in stark contrast to the target size predictions of 16 bases for BPS and 195 bases for indels. This result implies that indel mutations are much less probable than BPS [as also found by Lang and Murray (35)]. We can use this discrepancy to estimate the relative probability of the two major classes of mutation. This result reveals that the relative probability of substitution mutations is 0.95 [$f_{BPS} = (0.6/0.08)/((0.6/0.08) + 0.4)$], and that for the indels is 0.05 (f_{indels}), which is again in agreement with the data of Lang and Murray. Combining the target sizes with these relative probabilities of mutation gives us a final effective target size of $(\tau_{BPS} \times f_{BPS}) + (\tau_{indels} \times f_{indels}) = 25$ base pairs.

We can now combine the final effective target size with our earlier estimate of the number of mutations per experiment, which predicts that there should be ~510 loss-of-function mutations in *rsmE* per experiment. Although lower than the naive estimate of 4,000 mutations, this value is still well above the observed mutation rate of ~80 mutations per experiment. Therefore, we conclude that there is no clear evidence of a raised mutation rate in *rsmE* and that the emergence of *rsmE* mutants is better explained by the observed strong natural selection (Fig. 1).

Comparison of Emergence Rates Between Mucoid Variants. The frequencies with which we find the different mutants are extremely variable (Tables S1 and S2). For example, nonsense mutants tend to be underrepresented relative to missense mutants. As such, we were interested in whether some of the strong competitors exhibited differences in phenotype during the isolation process that we do not see in our other phenotypic assays. We, therefore, compared the relative proportions of emergence among the individual MVs using the same technique as described for Fig. S1*H*. We compared the proportion of emergence in WT colonies spiked with known number of MV cells. Competition experiments were set up on PAF plates between the selected MV and WT tagged with either GFP (WTG) or YFP (WTY) using mixtures set at the ratio (WT:MV) of $1:3 \times 10^{-6}$. The initial population size of each MV (69 ± 5; mean ± 95% confidence interval) was estimated by plating out the serially diluted culture before mixing with WTG or WTY. Previous experiments revealed that the optimal time point for assessing emergence was 3 d following inoculation (Fig. S1*H*).

Six independent competitions were set up for each MV against WTG or WTY. Colonies were visualized by fluorescent microscopy and the discrete nonfluorescent MV subcolonies were counted. There were no significant differences between the WTG and WTY competitions (nonparametric Mann–Whitney test, with Bonferroni correction for multiple comparisons, all $P > 0.0023$), so the results were averaged across all 12 competitions for each MV strain. The relative proportions of each introduced MV cells that emerged from the WT population are summarized in Fig. S5. Given the small sample size of 12 for each competition, a nonparametric Mann–Whitney test was applied. The data show a high variance and so are not definitive. Nevertheless, they are consistent with the view that all strong competitor mutants behave similarly in the emergence assay because we did not find large or significant differences among the different mutants tested. The one exception is the L23P mutant, a weak competitor phenotype, which had a significantly weaker emergence rate than some of the other mutants in the pairwise comparisons ($P < 0.05$).

1. Compeau G, Al-Achi BJ, Platsouka E, Levy SB (1988) Survival of rifampin-resistant mutants of *Pseudomonas fluorescens* and *Pseudomonas putida* in soil systems. *Appl Environ Microbiol* 54(10):2432–2438.
2. Simon R, Priefer U, Pühler A (1983) A broad host range mobilization system for in vivo genetic engineering: Transposon mutagenesis in Gram negative bacteria. *Nat Biotechnol* 1:784–791.
3. Kirner S, et al. (1996) The non-haem chloroperoxidase from *Pseudomonas fluorescens* and its relationship to pyrrolnitrin biosynthesis. *Microbiology* 142(Pt 8):2129–2135.
4. King EO, Ward MK, Raney DE (1954) Two simple media for the demonstration of pyocyanin and fluorescin. *J Lab Clin Med* 44(2):301–307.
5. Lenski RE, Rose MR, Simpson SC, Tadler SC (1991) Long-term experimental evolution in *Escherichia coli*. I. Adaptation and divergence during 2,000 generations. *Am Nat* 138(6):1315–1341.
6. Silby MW, et al. (2009) Genomic and genetic analyses of diversity and plant interactions of *Pseudomonas fluorescens*. *Genome Biol* 10(5):R51.
7. Huang W, Marth G (2008) EagleView: A genome assembly viewer for next-generation sequencing technologies. *Genome Res* 18(9):1538–1543.
8. Altschul SF, Gish W, Miller W, Myers EW, Lipman DJ (1990) Basic local alignment search tool. *J Mol Biol* 215(3):403–410.
9. Lapouge K, Schubert M, Allain FH-T, Haas D (2008) Gac/Rsm signal transduction pathway of gamma-proteobacteria: From RNA recognition to regulation of social behaviour. *Mol Microbiol* 67(2):241–253.
10. Horton RM, Hunt HD, Ho SN, Pullen JK, Pease LR (1989) Engineering hybrid genes without the use of restriction enzymes: Gene splicing by overlap extension. *Gene* 77(1):61–68.
11. Silby MW, Levy SB (2004) Use of in vivo expression technology to identify genes important in growth and survival of *Pseudomonas fluorescens* Pf0-1 in soil: Discovery of expressed sequences with novel genetic organization. *J Bacteriol* 186(21):7411–7419.
12. Shanks RMQ, Caiazza NC, Hinsa SM, Toutain CM, O'Toole GA (2006) *Saccharomyces cerevisiae*-based molecular tool kit for manipulation of genes from Gram-negative bacteria. *Appl Environ Microbiol* 72(7):5027–5036.

13. Kim W, Levy SB (2008) Increased fitness of *Pseudomonas fluorescens* Pf0-1 leucine auxotrophs in soil. *Appl Environ Microbiol* 74(12):3644–3651.
14. Silby MW, Nicoll JS, Levy SB (2009) Requirement of polyphosphate by *Pseudomonas fluorescens* Pf0-1 for competitive fitness and heat tolerance in laboratory media and sterile soil. *Appl Environ Microbiol* 75(12):3872–3881.
15. Lambertsen L, Sternberg C, Molin S (2004) Mini-Tn7 transposons for site-specific tagging of bacteria with fluorescent proteins. *Environ Microbiol* 6(7):726–732.
16. Nadell CD, Xavier JB, Levin SA, Foster KR (2008) The evolution of quorum sensing in bacterial biofilms. *PLoS Biol* 6(1):e14.
17. Xavier JB, Foster KR (2007) Cooperation and conflict in microbial biofilms. *Proc Natl Acad Sci USA* 104(3):876–881.
18. Nadell CD, Foster KR, Xavier JB (2010) Emergence of spatial structure in cell groups and the evolution of cooperation. *PLOS Comput Biol* 6(3):e1000716.
19. Schluter J, Foster KR (2012) The evolution of mutualism in gut microbiota via host epithelial selection. *PLoS Biol* 10(11):e1001424.
20. Mitri S, Xavier JB, Foster KR (2011) Social evolution in multispecies biofilms. *Proc Natl Acad Sci USA* 108(Suppl 2):10839–10846.
21. Korolev KS, Xavier JB, Nelson DR, Foster KR (2011) A quantitative test of population genetics using spatiogenetic patterns in bacterial colonies. *Am Nat* 178(4):538–552.
22. Nadell CD, Bassler BL (2011) A fitness trade-off between local competition and dispersal in *Vibrio cholerae* biofilms. *Proc Natl Acad Sci USA* 108(34):14181–14185.
23. Xavier JB, Picioreanu C, van Loosdrecht MCM (2005) A framework for multidimensional modelling of activity and structure of multispecies biofilms. *Environ Microbiol* 7(8):1085–1103.
24. Xavier JB, De Kreuk MK, Picioreanu C, Van Loosdrecht MCM (2007) Multi-scale individual-based model of microbial and bioconversion dynamics in aerobic granular sludge. *Environ Sci Technol* 41(18):6410–6417.
25. Kreft JU, Picioreanu C, Wimpenny JW, van Loosdrecht MC (2001) Individual-based modelling of biofilms. *Microbiology* 147(Pt 11):2897–2912.
26. Lardon LA, et al. (2011) iDynoMiCS: Next-generation individual-based modelling of biofilms. *Environ Microbiol* 13(9):2416–2434.
27. Rani SA, et al. (2007) Spatial patterns of DNA replication, protein synthesis, and oxygen concentration within bacterial biofilms reveal diverse physiological states. *J Bacteriol* 189(11):4223–4233.
28. Walters MC, 3rd, Roe F, Bugnicourt A, Franklin MJ, Stewart PS (2003) Contributions of antibiotic penetration, oxygen limitation, and low metabolic activity to tolerance of *Pseudomonas aeruginosa* biofilms to ciprofloxacin and tobramycin. *Antimicrob Agents Chemother* 47(1):317–323.
29. Schneider CA, Rasband WS, Eliceiri KW (2012) NIH Image to ImageJ: 25 years of image analysis. *Nat Methods* 9(7):671–675.
30. Xavier JB, Kim W, Foster KR (2011) A molecular mechanism that stabilizes cooperative secretions in *Pseudomonas aeruginosa*. *Mol Microbiol* 79(1):166–179.
31. Peters AC, Wimpenny JW, Coombs JP (1987) Oxygen profiles in, and in the agar beneath, colonies *of Bacillus cereus*, *Staphylococcus albus* and *Escherichia coli*. *J Gen Microbiol* 133(5):1257–1263.
32. Wimpenny JW, Lewis MW (1977) The growth and respiration of bacterial colonies. *J Gen Microbiol* 103(1):9–18.
33. Pirt SJ (1967) A kinetic study of the mode of growth of surface colonies of bacteria and fungi. *J Gen Microbiol* 47(2):181–197.
34. Drake JW, Charlesworth B, Charlesworth D, Crow JF (1998) Rates of spontaneous mutation. *Genetics* 148(4):1667–1686.
35. Lang GI, Murray AW (2008) Estimating the per-base-pair mutation rate in the yeast *Saccharomyces cerevisiae*. *Genetics* 178(1):67–82.

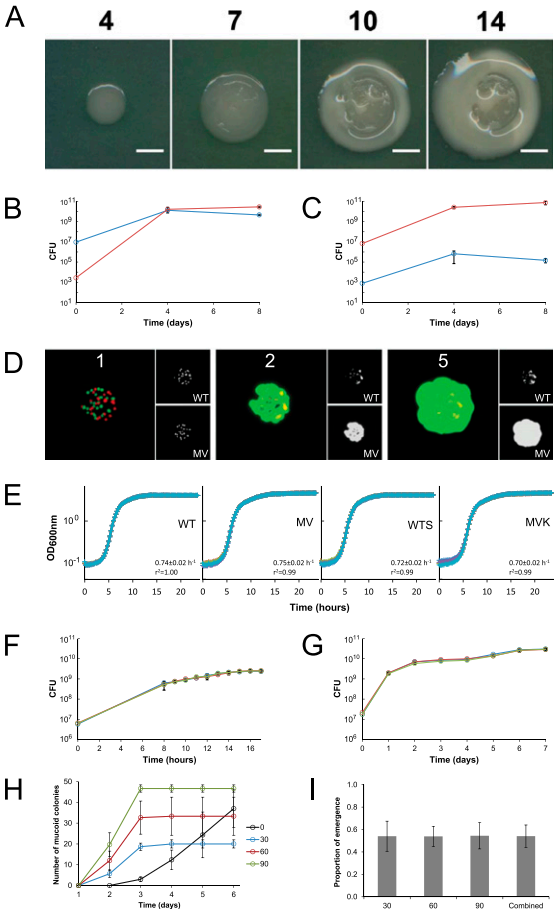

Fig. S1. Emergence of MV and comparison of MV and WT growth in single genotype and mixed cultures. (*A*) Emergence of mucoid variants in a colony initiated from a single WT cell. An isolated colony on PAF derived from serially diluting and plating out WT was observed over time (shown above each panel is the number of days postinoculation). (Scale bars, 5 mm.) (*B* and *C*) MV dominates WT in mixed colonies independent of the initial frequency. Results of competitions between MV and WT, where MV was initially underrepresented (*B*) or overrepresented (*C*) by 1,000-fold. The graphs show the mean population size of MV (red circle) and WT (blue circle) in CFU obtained from destructively sampling three independent populations at each interval. (*D*) Visual presentation of competition between fluorescently tagged MV (green) and WT (red) each starting at a low frequency. Both strains were diluted 10^{-5} from the stock preparations before mixing and imaged over time (number of days postinoculation). Shown are individual and overlay of images obtained from scanning with red and green lasers. (*E*) Growth profiles of single genotypes in in liquid KMB as measured by optical density at 600 nm. Genotypes are WT, streptomycin resistance tagged WT (WTS), MV, and kanamycin resistance tagged MV (MVK). Results from six replicates are shown in each graph along with the mean doubling time ± 95% confidence interval, and the regression coefficient of the data points used to calculate the doubling time. (*F* and *G*) Growth profiles of single genotype colonies on PAF plates in short (*F*) and long (*G*) timescales. Genotypes are WT (blue), MV (red), and Δ*rsmE* (green). The datapoints represent the mean CFU estimated from destructively sampling three populations. (*H*) Rate of emergence of MV from WT colonies where differing numbers of MV are spiked in at the start. Zero or ~30, 60, or 90 GFP-tagged MV (MVG) cells were mixed with WT. The zero case shows the rate of emergence of de novo mutants, whereas the GFP-spiking treatments show the rate of emergence of MV cells that are there from the beginning. Each datapoint represents the mean from three independent populations. (*I*) Graph depicting the mean proportion of patches observed after 6 d of incubation from the estimated number of introduced MVG cells. The initial frequency of introduced MVG cells for each competition is indicated below the *x* axis. The mean is from nine independent competitions and the mean from all 27 experiments combined is shown at the far right. Error bars represent the 95% confidence interval (*B*, *C*, *F*, and *G*) or the SD (*H* and *I*) of the mean.

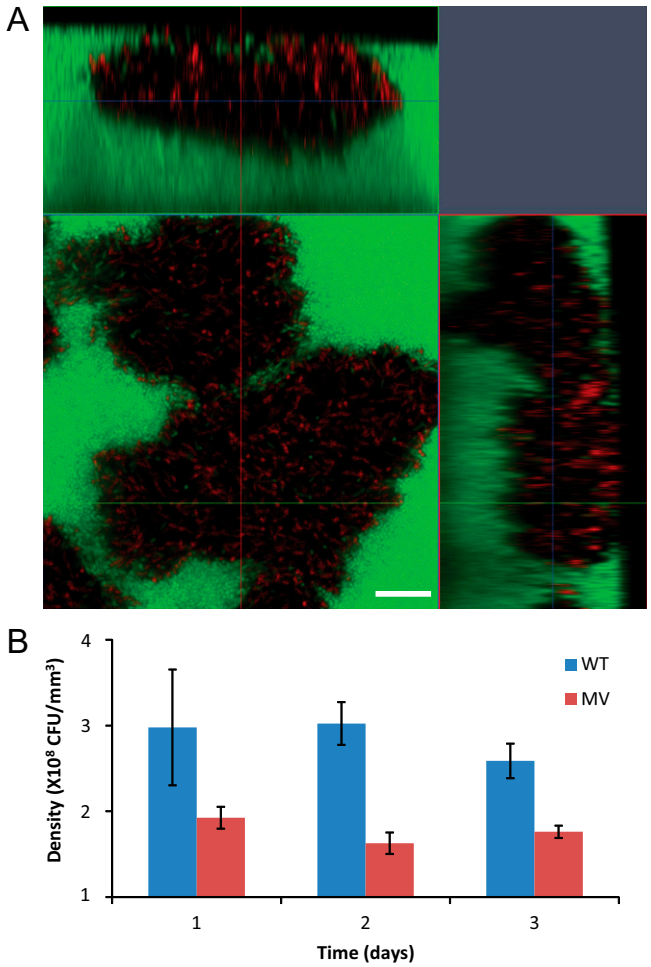

Fig. S2. Confocal laser scanning microscopy images of mixed colonies and estimation of population density in single genotype colonies. (*A*) Cells tend to align vertically in regions of competition between the genotypes. Mixed populations of fluorescently tagged Δ*rsmE* (DsRed-Express) and WT (GFP) were seeded at the initial ratio of 10^{-5}:1 (Δ*rsmE*:WT) and are imaged here on day 4. (Scale bar, 10 μm.) (*B*) Comparison of density differences between unmixed WT and MV colonies over time. Density was estimated by combining confocal microscopy estimates of colony volume with destructive sampling to obtain cell number at each time point. Error bars represent the SD of the mean of three colonies. The *P* values obtained from a two-tailed *t* test were 0.0554, 0.001, and 0.0025 over the 3 d, respectively.

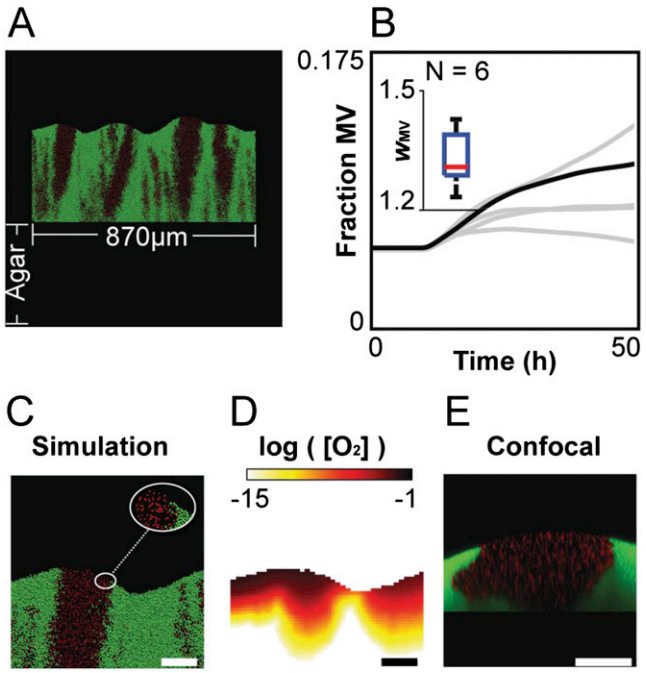

Fig. S3. Individual-based simulations with cell division at a random angle. (*A*) Snapshot from a 2D simulation of an 870-μm-wide cross-section of a colony growing on agar; MV in red, WT in green. (*B*) Fraction of the mucoid variant of total biomass over 50 h in six independent simulations (black line: simulation shown in *A*, *C*, and *D*); initial fraction 0.05. (*Inset*) The MV is fitter than the WT. The boxplot shows the relative fitness (W) of the MV at $t = 50$ h; the asterisk (*) means results significantly different from equal fitness ($W = 1$), Wilcoxon signed-rank test ($P = 0.0313$). (*C*) Close-up of a region from the simulated colony. Because of the secretion of polymers, mucoid variant cells are less densely packed than WT cells. (*D*) Oxygen concentration profile in the simulation of the region shown in *C*. More oxygen is available in the region of mucoid variant cells because of the lower local cell density. (*E*) Confocal microscopy image of a colony of MV cells expressing DsRed-Express and WT cells expressing GFP. (Scale bars, 50 μm.)

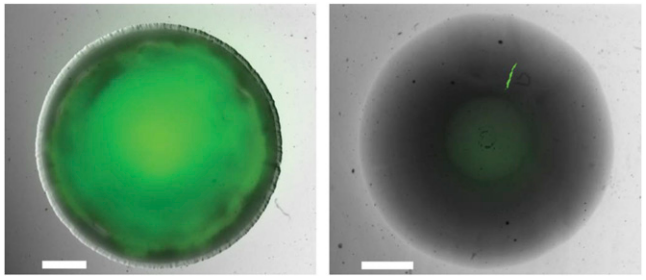

Fig. S4. Effect of limiting upward expansion on competitive ability of Δ*rsmE*. GFP-tagged Δ*rsmE* was mixed with unlabeled WT at a starting ratio of 10^{-2}:1. After spotting the mixture on the agar surface, colonies were incubated either undisturbed (*Left*) or covered with a thin layer of agarose (*Right*). Images were captured after four days of incubation by fluorescent microscopy. (Scale bars, 2 mm.)

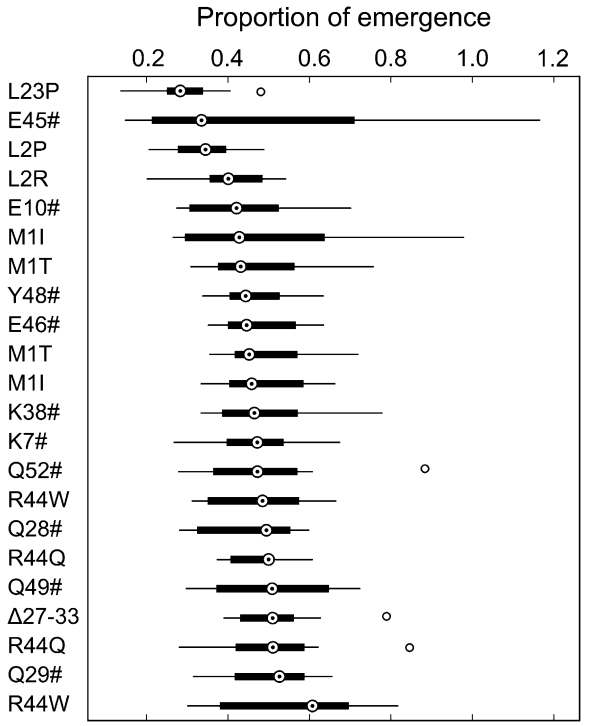

Fig. S5. Comparison of emergence of various MVs from spiked WT populations. A boxplot illustrating the distribution of proportions of MVs that emerged 3 d after mixing ~70 CFU with dense population of WT (~10^7 CFU). WT was tagged with YFP or GFP and the MVs were untagged, thus nonfluorescent patches that emerged were counted. Each box plot shows the median (inner circle), upper and lower quartiles (edges of box), and outliers (outer circle) among 12 replicates. Multiple occurrences of the same genotype indicate independently isolated mutants. According to a nonparametric Mann–Whitney test ($n = 12$, $P < 0.05$), only the L23P mutant showed any differences among the group.

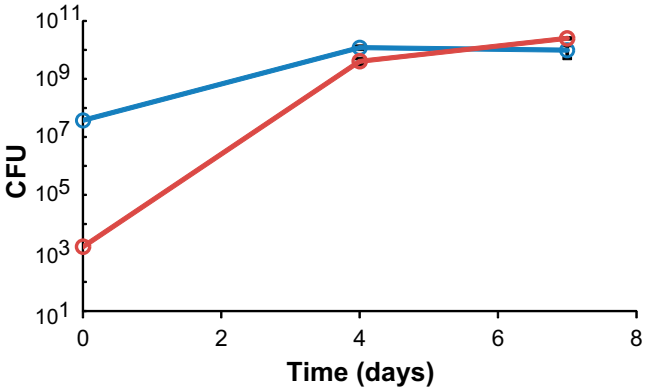

Fig. S6. Loss of flagella has no bearing on MV's fitness. Results of competitions between MV(Δ*fliC*) and WT commenced at 10^{-5}:1 ratio. WT was tagged with streptomycin resistance and MV(Δ*fliC*) was tagged with kanamycin resistance. The graph shows the mean population size of MV(Δ*fliC*) (red circle) and WT (blue circle) in CFU obtained from destructively sampling three independent populations at each interval. Error bars represent the 95% confidence interval.

Table S1. Summary of mutations identified in the parallel evolution study

Location[†]	Mutation[‡]	Consequence[§]	Genotype[¶]	Frequency
U->65	Δ268	Entire gene deletion	Δ-17-(ORF+56)	1
U-65	Δ299	Partial gene deletion	Δ-106-193	1
U-59	Δ360	Partial gene deletion	Δ-184-176	1
U-45	Δ260	Partial gene deletion	Δ-125-135	1
U-42	Δ207	Partial gene deletion	Δ-81-126	1
U-40	Δ133	Partial gene deletion	Δ-13-120	1
U-14	Δ51	Partial gene deletion	Δ-11-40	1
U-10	Δ40	Partial gene deletion	Δ-10-30	1
U-6	Δ324	Partial gene deletion	Δ-307-17	1
U	Δ149	Upstream deletion	Δ-161-(-13)	2
U	Δ149	Upstream deletion	Δ-155-(-7)	1
U	Δ119	Upstream deletion	Δ-132-(-14)	1
U	Δ77	Upstream deletion	Δ-80-(-4)	1
U	G→A	Substitution (5′ UTR)	G→A (-30)	1
U	T→A	Substitution (5′ UTR)	T→A (-29)	6
U	A→C	Substitution (5′ UTR)	A→C (-23)	5
U	CTACA→CTA([*IS*]CTA)CA[‖]	Disrupted 5′ UTR (IS)	*IS*+3 (-22)	1
U	A→G	Substitution (5′ UTR)	A→G (-19)	3
U	A→C	Substitution (5′ UTR)	A→C (-15)	1
U	AAGGAGA→A*****A	Disrupted SD	Δ-11-(-7)	1
U	AAGGAGA→AAGAAGA	Disrupted SD	G→A (-9)	8
1	ATG→CTG	Missense (START lost)	M1L	3
1	ATG→AAG	Missense (START lost)	M1K	1
1	ATG→AGG	Missense (START lost)	M1R	3
1	ATG→ACG	Missense (START lost)	M1T	9
1	ATG→ATA	Missense (START lost)	M1I	51
1	ATG→ATT	Missense (START lost)	M1I	3
1	ATG→ATC	Missense (START lost)	M1I	1
1	ATG→A([*IS*]CCA)TG[‖]	Frameshift (IS)	M1M+IS+4	1
1–3	Δ5	Frameshift (deletion)	Δ3–7	1
1–5	Δ15	In-frame deletion	Δ1–15	1
2	CTG→CCG	Missense	L2P	6
2	CTG→CAG	Missense	L2Q	2
2	CTG→CGG	Missense	L2R	3
2	CTG→(T)CTG	Frameshift (insertion)	L2S+1	1
2	CTG→CT(CT)G	Frameshift (insertion)	L2L+2	1
3	ATA→A(C)TA	Frameshift (insertion)	I3T+1	1
3	ATA→AT*	Frameshift (deletion)	Δ9	4
4	CTC→CCC	Missense	L4P	62
4	CTC→(A)CTC	Frameshift (insertion)	L4T+1	1
5	ACC→CCC	Missense	T5P	6
6	CGC→CAC	Missense	R6H	2
6	CGC→*GC	Frameshift (deletion)	Δ16	1
7	AAA→TAA	Nonsense	K7#	6
7	AAA→(T)AAA	Frameshift (insertion)	K7#+1	1
7	AAA→AA*	Frameshift (deletion)	Δ21	2
7–11	Δ13	Frameshift (deletion)	Δ20–32	1
7–11	Δ11	Frameshift (deletion)	Δ21–31	2
8	GTC→(C)GTC	Frameshift (insertion)	V8R+1	1
8	GTC→(A)GTC	Frameshift (insertion)	V8S+1	1
8	GTC→*TC	Frameshift (deletion)	Δ22	1
8–25	Δ52	In-frame deletion	Δ22–73	2
8–38	Δ91	Frameshift (deletion)	Δ22–112	1
9	GGT→(G)GGT	Frameshift (insertion)	G9G+1	1
9–11	Δ7	Frameshift (deletion)	Δ27–33	1
10	GAA→TAA	Nonsense	E10#	2
10	GAA→GA*	Frameshift (deletion)	Δ30	2
10–14	Δ11	Frameshift (deletion)	Δ30–40	2
11	AGC→AG([*IS*]AAG)C[d]	Frameshift (IS)	S11S+*IS*+3	2
11–14	Δ10	Frameshift (deletion)	Δ32–41	4
11–14	Δ11	Frameshift (deletion)	Δ32–42	4
12	ATA→AT*	Frameshift (deletion)	Δ36	2
13	AAC→AA(A)C	Frameshift (insertion)	N13K+1	1

Table S1. Cont.

Location[†]	Mutation[‡]	Consequence[§]	Genotype[¶]	Frequency
13	AAC→A*C	Frameshift (deletion)	Δ38	1
13	AAC→AA*	Frameshift (deletion)	Δ39	5
13–14	Δ4	Frameshift (deletion)	Δ39–42	1
14	ATT→AAT	Missense	I14N	1
14–15	Δ4	Frameshift (deletion)	Δ40–43	1
20	ATC→AGC	Missense	I20S	1
21	ACC→CCC	Missense	T21P	2
22	ATT→AT(C)T	Frameshift (insertion)	I22I+1	1
22–30	Δ25	Frameshift (deletion)	Δ64–88	1
23	CTC→C(GACATCACGATCACCATTC)TC	Frameshift (insertion)	L23R+19	1
23	CTC→CCC	Missense	L23P	6
24–33	Δ27	Frameshift (deletion)	Δ71–97	1
25–31	Δ16	Frameshift (deletion)	Δ74–89	1
25–31	Δ19	Frameshift (deletion)	Δ74–92	1
27	GGC→GG*	Frameshift (deletion)	Δ81	2
28	CAG→TAG	Nonsense	Q28#	3
28	CAG→*AG	Frameshift (deletion)	Δ82	1
29	CAA→TAA	Nonsense	Q29#	11
29	CAA→CA*	Frameshift (deletion)	Δ87	1
29–50	Δ63	In-frame deletion	Δ86–148	1
31	CGA→TGA	Nonsense	R31#	4
32	ATC→AAC	Missense	I32N	1
34	ATC→*TC	Frameshift (deletion)	Δ100	1
34	ATC→AT*	Frameshift (deletion)	Δ102	1
34–37	Δ10	Frameshift (deletion)	Δ100–109	1
34–39	Δ15	In-frame deletion	Δ102–116	1
36	GCT→(T)GCT	Frameshift (insertion)	A36C+1	1
36	GCT→*CT	Frameshift (deletion)	Δ106	5
36	GCT→G*T	Frameshift (deletion)	Δ107	3
36	Δ2	Frameshift (deletion)	Δ106–107	4
36	Δ3	In-frame deletion	Δ106–108	1
36–37	Δ5	Frameshift (deletion)	Δ106–110	1
36–38	Δ9	In-frame deletion	Δ106–114	1
36–39	Δ11	Frameshift (deletion)	Δ106–116	2
36–39	Δ12	In-frame deletion	Δ106–117	1
36–39	Δ9	In-frame deletion	Δ107–115	1
36–39	Δ10	Frameshift (deletion)	Δ107–116	2
36–39	Δ11	Frameshift (deletion)	Δ107–117	3
36–40	Δ12	In-frame deletion	Δ107–118	5
36–41	Δ17	Frameshift (deletion)	Δ106–122	1
37	CCG→C([*IS*]CTC)CG[‖]	Frameshift (IS)	P37L+*IS*+3	3
37	CCG→C(CGAAGAA)CG	Frameshift (insertion)	P37P+7	1
37	CCG→C*G	Frameshift (deletion)	Δ110	1
37–39	Δ5	Frameshift (deletion)	Δ111–115	1
38	AAG→TAG	Nonsense	K38#	1
38	AAG→A*G	Frameshift (deletion)	Δ113	1
38–42	Δ15	In-frame deletion	Δ112–126	3
39–41	Δ5	Frameshift (deletion)	Δ117–121	1
39–42	Δ10	Frameshift (deletion)	Δ116–125	1
40	GTT→GT*	Frameshift (deletion)	Δ120	15
40–41	Δ4	Frameshift (deletion)	Δ119–122	1
40–41	Δ2	Frameshift (deletion)	Δ120–121	2
40–43	Δ11	Frameshift (deletion)	Δ119–128	1
40–44	Δ13	Frameshift (deletion)	Δ119–131	3
40–45	Δ15	In-frame deletion	Δ119–133	1
41	GCA→*CA	Frameshift (deletion)	Δ121	24
41	GCA→G*A	Frameshift (deletion)	Δ122	3
41	Δ2	Frameshift (deletion)	Δ121–122	2
42	GTA→GAA	Missense	V42E	10
42	GTA→GT*	Frameshift (deletion)	Δ126	6
42–43	Δ3	In-frame deletion	Δ125–127	1
42–46	Δ11	Frameshift (deletion)	Δ126–136	2

Table S1. Cont.

Location[†]	Mutation[‡]	Consequence[§]	Genotype[¶]	Frequency
43	CAC→CCC	Missense	H43P	1
43	CAC→*AC	Frameshift (deletion)	Δ127	5
43–46	Δ10	Frameshift (deletion)	Δ127–136	1
43–47	Δ14	Frameshift (deletion)	Δ128–141	1
43–48	Δ16	Frameshift (deletion)	Δ127–142	1
44	CGG→TGG	Missense	R44W	12
44	CGG→CCG	Missense	R44P	1
44	CGG→CAG	Missense	R44Q	69
45	GAA→TAA	Nonsense	E45#	2
45	GAA→GA(GT)A	Frameshift (insertion)	E45E+2	1
46	GAG→TAG	Nonsense	E46#	3
47	ATC→*TC	Frameshift (deletion)	Δ139	9
48	TAC→TAG	Nonsense	Y48#	5
48	TAC→*AC	Frameshift (deletion)	Δ142	1
48–49	Δ4	Frameshift (deletion)	Δ142–145	1
49	CAG→TAG	Nonsense	Q49#	1
49	CAG→(T)CAG	Frameshift (insertion)	Q49S+1	1
49	CAG→*AG	Frameshift (deletion)	Δ145	1
49–53	Δ14	Frameshift (deletion)	Δ145–158	1
49–53	Δ13	Frameshift (deletion)	Δ146–158	1
49–54	Δ16	Frameshift (deletion)	Δ145–160	1
50–51	Δ2	Frameshift (deletion)	Δ150–151	1
52	Δ2	Frameshift (deletion)	Δ155–156	1
52	CAG→TAG	Nonsense	Q52#	2
53–56	Δ11	Frameshift (deletion)	Δ157–167	1
54	GGC→G*C	Frameshift (deletion)	Δ161	2
57–61	Δ11	In-frame deletion	Δ171–181	1
59–61	Δ5	Frameshift (deletion)	Δ177–181	1
61	CCA→(G)CCA	Frameshift (insertion)	P61A+1	1
65	TGA→CGA	Missense (STOP lost)	#65R	24
65	TGA→TTA	Missense (STOP lost)	#65L	1
65	TGA→TGG	Missense (STOP lost)	#65W	1

Each variant was isolated from a unique WT population, with the exception of three belonging to the #65L, L4P, and Δ-11-(-7) genotypes that were isolated from discrete patches emerging from a common WT population.

[†]Location of mutation with respect to the relative positions within the amino acid sequence; U denotes the region upstream from the START site; U->65 denotes the entire ORF and flanking regions.

[‡]Changes in the nucleotide sequence; * denotes a single nucleotide deletion; Δ denotes the number of nucleotides deleted; inserted nucleotides are indicated within parentheses; underlined nucleotides represent the Shine-Dalgarno sequence.

[§]Partial gene deletion includes coding and upstream regions; 5′ UTR denotes the five prime untranslated region; STOP lost mutation results in read through of 18 additional amino acids; SD denotes the Shine-Dalgarno sequence.

[¶]The # denotes a STOP codon; ΔN denotes the relative nucleotide positions of deletion within the coding sequence; position of mutations in the region upstream from the coding sequence is indicated within the parentheses relative to the START codon, and the nucleotide substitution is shown where applicable; + denotes the number of nucleotides inserted or an insertion sequence element.

[||]IS denotes the insertion of a 1,313-bp insertion sequence element. All but one share exact nucleotide sequence identity as those annotated in the WT genome as Pfl01_0068-0069 or Pfl01_1346-13477. There are two additional IS elements in the genome (Pfl01_2031-2032 and Pfl01_2130-2131) that differ by a single nucleotide. One of the three in the P37L+*IS*+3 genotype shares exact nucleotide sequence identity with those in the latter group.

Table S2. Summary of possible and identified substitutions within the coding sequence of *rsmE*

WT sequence			First position						Second position						Third position					
No.	Codon	AA	Ts		Tv		Tv		Ts		Tv		Tv		Ts		Tv		Tv	
1	ATG	M	GTG	V	CTG	L (3)	TTG	L	ACG	T (9)	AAG	K (1)	AGG	R (1)	ATA	I (51)	ATC	I (1)	ATT	I (3)
2	CTG	L	TTG	L	ATG	M	GTG	V	CCG	P (6)	CAG	Q (2)	CGG	R (3)	CTA	L	CTC	L	CTT	L
3	ATA	I	GTA	V	CTA	L	TTA	F	ACA	T	AAA	K	AGA	R	ATG	M	ATC	I	ATT	I
4	CTC	L	TTC	F	ATC	I	GTC	V	CCC	P (62)	CAC	H	CGC	R	CTT	L	CTA	L	CTG	L
5	ACC	T	GCC	A	CCC	P (6)	TCC	S	ATC	I	AAC	N	AGC	S	ACT	T	ACA	T	ACG	T
6	CGC	R	TGC	C	AGC	S	GGC	G	CAC	H (2)	CCC	P	CTC	L	CGT	R	CGA	R	CGG	R
7	(AAA)	K	GAA	E	CAA	Q	TAA	# (6)	AGA	R	ACA	T	ATA	I	AAG	K	AAC	N	AAT	N
8	GTC	V	ATC	I	CTC	L	TTC	F	GCC	A	GAC	D	GGC	G	GTT	V	GTA	V	GTG	V
9	GGT	G	AGT	S	CGT	R	TGT	C	GAT	D	GCT	A	GTT	V	GGC	G	GGA	G	GGG	G
10	(GAA)	E	AAA	K	CAA	Q	TAA	# (2)	GGA	G	GCA	A	GTA	V	GAG	E	GAC	D	GAT	D
11	AGC	S	GGC	G	CGC	R	TGC	C	AAC	N	ACC	T	ATC	I	AGT	S	AGA	R	AGG	R
12	ATA	I	GTA	V	CTA	L	TTA	F	ACA	T	AAA	K	AGA	R	ATG	M	ATC	I	ATT	I
13	AAC	N	GAC	D	CAC	H	TAC	Y	AGC	S	ACC	T	ATC	I	AAT	N	AAA	K	AAG	K
14	ATT	I	GTT	V	CTT	L	TTT	F	ACT	T	AAT	N (1)	AGT	S	ATC	I	ATA	I	ATG	M
15	GGT	G	AGT	S	CGT	R	TGT	C	GAT	D	GCT	A	GTT	V	GGC	G	GGA	G	GGG	G
16	GAT	D	AAT	N	CAT	H	TAT	Y	GGT	G	GCT	A	GTT	V	GAC	D	GAA	E	GAG	E
17	GAC	D	AAC	N	CAC	H	TAC	Y	GGC	G	GCC	A	GTC	V	GAT	D	GAA	E	GAG	E
18	ATC	I	GTC	V	CTC	L	TTC	F	ACC	T	AAC	N	AGC	S	ATT	I	ATA	I	ATG	M
19	ACG	T	GCG	A	CCG	P	TCG	S	ATG	M	AAG	K	AGG	R	ACA	T	ACC	T	ACT	T
20	ATC	I	GTC	V	CTC	L	TTC	F	ACC	T	AAC	N	AGC	S (1)	ATT	I	ATA	I	ATG	M
21	ACC	T	GCC	A	CCC	P (2)	TCC	S	ATC	I	AAC	N	AGC	S	ACT	T	ACA	T	ACG	T
22	ATT	I	GTT	V	CTT	L	TTT	F	ACT	T	AAT	N	AGT	S	ATC	I	ATA	I	ATG	M
23	CTC	L	TTC	F	ATC	I	GTC	V	CCC	P (6)	CAC	H	CGC	R	CTT	L	CTA	L	CTG	L
24	GGC	G	AGC	S	CGC	R	TGC	C	GAC	D	GCC	A	GTC	V	GGT	G	GGA	G	GGG	G
25	GTC	V	ATC	I	CTC	L	TTC	F	GCC	A	GAC	D	GGC	G	GTT	V	GTA	V	GTG	V
26	AGC	S	GGC	G	CGC	R	TGC	C	AAC	N	ACC	T	ATC	I	AGT	S	AGA	R	AGG	R
27	GGC	G	AGC	S	CGC	R	TGC	C	GAC	D	GCC	A	GTC	V	GGT	G	GGA	G	GGG	G
28	(CAG)	Q	TAG	# (3)	AAG	K	GAG	E	CGG	R	CCG	P	CTG	L	CAA	Q	CAC	H	CAT	H
29	(CAA)	Q	TAA	# (11)	AAA	K	GAA	E	CGA	R	CCA	P	CTA	L	CAG	Q	CAC	H	CAT	H
30	GTT	V	ATT	I	CTT	L	TTT	F	GCT	A	GAT	D	GGT	G	GTC	V	GTA	V	GTG	V
31	(CGA)	R	TGA	# (4)	AGA	R	GGA	G	CAA	Q	CCA	P	CTA	L	CGG	R	CGC	R	CGT	R
32	ATC	I	GTC	V	CTC	L	TTC	F	ACC	T	AAC	N (1)	AGC	S	ATT	I	ATA	I	ATG	M
33	GGC	G	AGC	S	CGC	R	TGC	C	GAC	D	GCC	A	GTC	V	GGT	G	GGA	G	GGG	G
34	ATC	I	GTC	V	CTC	L	TTC	F	ACC	T	AAC	N	AGC	S	ATT	I	ATA	I	ATG	M
35	AAT	N	GAT	D	CAT	H	TAT	Y	AGT	S	ACT	T	ATT	I	AAC	N	AAA	K	AAG	K
36	GCT	A	ACT	T	CCT	P	TCT	S	GTT	V	GAT	D	GGT	G	GCC	A	GCA	A	GCG	A
37	CCG	P	TCG	S	ACG	T	GCG	A	CTG	L	CAG	Q	CGG	R	CCA	P	CCC	P	CCT	P
38	(AAG)	K	GAG	E	CAG	Q	TAG	# (1)	AGG	R	ACG	T	ATG	M	AAA	K	AAC	N	AAT	N
39	AAC	N	GAC	D	CAC	H	TAC	Y	AGC	S	ACC	T	ATC	I	AAT	N	AAA	K	AAG	K
40	GTT	V	ATT	I	CTT	L	TTT	F	GCT	A	GAT	D	GGT	G	GTC	V	GTA	V	GTG	V
41	GCA	A	ACA	T	CCA	P	TCA	S	GTA	V	GAA	E	GGA	G	GCG	A	GCC	A	GCT	A
42	GTA	V	ATA	I	CTA	L	TTA	L	GCA	A	GAA	E (10)	GGA	G	GTG	V	GTC	V	GTT	V
43	CAC	H	TAC	Y	AAC	N	GAC	D	CGC	R	CCC	P (1)	CTC	L	CAT	H	CAA	Q	CAG	Q
44	CGG	R	TGG	W (12)	AGG	R	GGG	G	CAG	Q (69)	CCG	P (1)	CTG	L	CGA	R	CGC	R	CGT	R
45	(GAA)	E	AAA	K	CAA	Q	TAA	# (2)	GGA	G	GCA	A	GTA	V	GAG	E	GAC	D	GAT	D
46	(GAG)	E	AAG	K	CAG	Q	TAG	# (3)	GGG	G	GCG	A	GTG	V	GAA	E	GAC	D	GAT	D
47	ATC	I	GTC	V	CTC	L	TTC	F	ACC	T	AAC	N	AGC	S	ATT	I	ATA	I	ATG	M
48	(TAC)	Y	CAC	H	AAC	N	GAC	D	TGC	C	TCC	S	TTC	F	TAT	Y	TAA	#	TAG	# (5)
49	(CAG)	Q	TAG	# (1)	AAG	K	GAG	E	CGG	R	CCG	P	CTG	L	CAA	Q	CAC	H	CAT	H

Table S2. Cont.

WT sequence			First position						Second position						Third position					
No.	Codon	AA	Ts		Tv		Tv		Ts		Tv		Tv		Ts		Tv		Tv	
50	CGC	R	TGC	C	AGC	S	GGC	G	CAC	H	CCC	P	CTC	L	CGT	R	CGA	R	CGG	R
51	ATC	I	GTC	V	CTC	L	TTC	F	ACC	T	AAC	N	AGC	S	ATT	I	ATA	I	ATG	M
52	(CAG)	Q	TAG	# (2)	AAG	K	GAG	E	CGG	R	CCG	P	CTG	L	CAA	Q	CAC	H	CAT	H
53	GCG	A	ACG	A	CCG	P	TCG	S	GTG	V	GAG	E	GGG	G	GCA	A	GCC	A	GCT	A
54	GGC	G	AGC	S	CGC	R	TGC	C	GAC	D	GCC	A	GTC	V	GGT	G	GGA	G	GGG	G
55	CTG	L	TTG	L	ATG	M	GTG	V	CCG	P	CAG	Q	CGG	R	CTA	L	CTC	L	CTT	L
56	ACC	T	GCC	A	CCC	P	TCC	S	ATC	I	AAC	N	AGC	S	ACT	T	ACA	T	ACG	T
57	GCT	A	ACT	T	CCT	P	TCT	S	GTT	V	GAT	D	GGT	G	GCC	A	GCA	A	GCG	A
58	CCG	P	TCG	S	ACG	T	GCG	A	CTG	L	CAG	Q	CGG	R	CCA	P	CCC	P	CCT	P
59	GAC	D	AAC	N	CAC	H	TAC	Y	GGC	G	GCC	A	GTC	V	GAT	D	GAA	E	GAG	E
60	(AAG)	K	GAG	E	CAG	Q	TAG	#	AGG	R	ACG	T	ATG	M	AAA	K	AAC	N	AAT	N
61	CCA	P	TCA	S	ACA	T	GCA	A	CTA	L	CAA	Q	CGA	R	CCG	P	CCC	P	CCT	P
62	(CAA)	Q	TAA	#	AAA	K	GAA	E	CGA	R	CCA	P	CTA	L	CAG	Q	CAC	H	CAT	H
63	ACG	T	GCG	A	CCG	P	TCG	S	ATG	M	AAG	K	AGG	R	ACA	T	ACC	T	ACT	T
64	CCT	P	TCT	S	ACT	T	GCT	A	CTT	L	CAT	H	CGT	R	CCC	P	CCA	P	CCG	P
65	TGA	#	CGA	R (24)	AGA	R	GGA	G	TAA	#	TCA	S	TTA	L (1)	TGG	W (1)	TGC	C	TGT	C

Possible substitutions and corresponding amino acid changes are grouped based on the three positions of the codon; Ts denotes transition and Tv denotes transversion; codons within parentheses are pretermination codons and # denotes the STOP codon; identified substitutions are highlighted and frequency noted within parentheses; substitutions highlighted in red or blue resulted in large or reduced colony spreading, respectively, as shown in Fig. 6. Robustness was calculated as follows: [8 (number of observed missense substitutions that resulted in a knock-out phenotype (i.e., highlighted in red), excluding the START/STOP codons) / 0.95 (estimation of missense coverage based on nonsense and START codon mutation identification)]/409 (total number of possible missense substitutions available, excluding the nonsense and START/STOP codons) = 2%.

Table S3. Parameters used in the individual-based simulations

Parameter	Value	Source
Diffusion coefficient O_2	7.2e6 ($\mu m^2/h$)	(1)
Monod constant O_2	3.5e-5 (g/L)	(2)
Maximum growth rate cells	0.5 (h^{-1})	Approximated
Specific masses		(2)
Cells	220 [g(carbon)/L]	
Polymer	44 [g(carbon)/L]	
Maximum cell diameter	1 (μm)	
Boundary conditions		
Periodic boundaries at the sides		
O_2 concentrations bulk air/colony boundary layer interface	8.90e-3 (g/L)	(3)
O_2 concentration bulk agar below 250 μm	8.90e-4 (g/L)	(1, 3–6)

1. Picioreanu C, Vanloosdrecht M, Heijnen J (1997) Modelling the effect of oxygen concentration on nitrite accumulation in a biofilm airlift suspension reactor. *Water Sci Technol* 36(1):147–156.
2. Nadell CD, Xavier JB, Levin SA, Foster KR (2008) The evolution of quorum sensing in bacterial biofilms. *PLoS Biol* 6(1):e14.
3. Xavier JB, Foster KR (2007) Cooperation and conflict in microbial biofilms. *Proc Natl Acad Sci USA* 104(3):876–881.
4. Rani SA, et al. (2007) Spatial patterns of DNA replication, protein synthesis, and oxygen concentration within bacterial biofilms reveal diverse physiological states. *J Bacteriol* 189(11): 4223–4233.
5. Walters MC, 3rd, Roe F, Bugnicourt A, Franklin MJ, Stewart PS (2003) Contributions of antibiotic penetration, oxygen limitation, and low metabolic activity to tolerance of *Pseudomonas aeruginosa* biofilms to ciprofloxacin and tobramycin. *Antimicrob Agents Chemother* 47(1):317–323.
6. Peters AC, Wimpenny JW, Coombs JP (1987) Oxygen profiles in, and in the agar beneath, colonies of *Bacillus cereus*, *Staphylococcus albus* and *Escherichia coli*. *J Gen Microbiol* 133(5): 1257–1263.